Word count: about 8900

Revision 3

Vanadium-induced coloration in grossite ($CaAl_4O_7$) and hibonite ($CaAl_{12}O_{19}$)

Matteo Ardit[a,*], Fernando Cámara[b] and Ulf Hålenius[c]

[a] Department of Physics and Earth Sciences, University of Ferrara, via Saragat 1, I-44122 Ferrara, Italy

[b] Department of Earth Sciences, University of Milano, Via Botticelli 23, I-20133 Milano, Italy

[c] Department of Geosciences, Swedish Museum of Natural History, P.O. Box 50 007, SE-104 05 Stockholm, Sweden

[*]Corresponding author, e-mail: rdtmtt@unife.it

address: via Saragat 1, I-44122 Ferrara, Italy

phone: +39(0)532 974732

co-author e-mails: fernando.camara@unimi.it, ulf.halenius@nrm.se

ABSTRACT

High concentrations of vanadium cause very unusual coloration in hibonite (purple) and grossite (light violet) crystals in an exotic mineral assemblage from Sierra de Comechingones (Argentina). In the hibonite ($CaAl_{12}O_{19}$) structure vanadium ions, in various valence states (divalent, trivalent and tetravalent), may be distributed over five crystallographic sites with coordinations corresponding to different polyhedra, namely, three unequal octahedra [*M*1 (D_{3d}), *M*4 (C_{3v}) and *M*5 (C_s)], one *M*3 tetrahedron (C_{3v}), and one unusual 5-fold coordinated trigonal bipyramid *M*2 (D_{3h}). Possible locations of vanadium ions in grossite ($CaAl_4O_7$) are limited to two crystallographically distinct sites (*T*1 and *T*2, both C_1) in tetrahedral coordination.

The combination of single-crystal X-ray diffraction and absorption spectroscopy techniques aided by chemical analyses has yielded details on the nature of the vanadium-induced color in both hibonite and grossite crystals. In hibonite, both *M*4 face-sharing octahedral and *M*2 trigonal bipyramid sites of the *R*-

block are partially occupied by V^{3+}. Strongly polarized bands recorded at relatively low energies in optical absorption spectra indicate that V^{2+} is located at the *M*4 octahedral site of the hibonite *R*-block. Chemical analyses coupled with an accurate determination of the electron densities at structural sites in hibonite suggest that the vanadium ions occupy about 10% and 5% of the *M*4 and *M*2 sites, respectively. For grossite, polarized optical absorption spectra reveal no indications of V^{2+}; all observed absorption bands can be assigned to V^{3+} in tetrahedral coordination. Although not evident by the observed electron densities at the *T* sites of grossite (due to the low V content), longer bond distances and a higher degree of polyhedral distortion suggest that V^{3+} is located at the *T*2 site.

***Keywords*:** calcium aluminates; hibonite; grossite; optical absorption spectroscopy; single-crystal X-ray diffraction; vanadium

INTRODUCTION

The importance of calcium-aluminum oxide compounds and mineralogical analogs evenly spans Materials Science and Earth Sciences. Hibonite (ideal formula $CaAl_{12}O_{19}$) and grossite (ideal formula $CaAl_4O_7$) are common constituents of calcium aluminate cements (CACs), which are a special type of cement commonly used in refractory concrete production. Along with the monocalcium aluminate ($CaAl_2O_4$, CA, also known as krotite) (Ma et al. 2011), which is the main and ubiquitous phase of all types of CACs, monocalcium dialuminate (grossite, CA2) and monocalcium hexa-aluminate (hibonite, CA6) are the main phases belonging to the so-called white cements, namely those cements containing >70 wt.% Al_2O_3 (Taylor 1997). Similarly, hibonite and grossite are important in Earth Sciences since they occur as mineral components of calcium aluminum rich inclusions (CAIs) in carbonaceous chondritic meteorites (Hofmeister et al. 2004; Hazen et al. 2008, and refs. therein). Being among the first

phases to crystallize during the first stages of nebula condensation, their investigation has provided, and still does, information about the conditions in the early solar nebula (Beckett et al. 1988; Brearley and Jones 1998).

Although both hibonite and grossite are very rarely reported in terrestrial occurrences, they have been found in some particular environments, e.g., in the pyrometamorphic rocks of the Hatrurim Formation, Israel (Gross 1977; Weber and Bischoff 1994). Hibonite is somehow more frequent but still rare in Earth if not related to meteorites. So far, it has been reported only in six localities: granulites from the type locality in Esiva eluvials in Madagascar (Delbos 1955), Furua granulites at the Ligama Hill, Morogoro Region, Tanzania (Masskant et al. 1980), Mg-Al skarn iron deposits of the Fushan Mine, She County, Hebei, Handan, China (Cao et al. 1997), Chyulu Hills volcanic field, Kenya (Ulianov et al. 2005), Mandalay region of Myanmar (Nagashima et al. 2010; Wild and Milisenda 2013), and Tashelginskoye Fe-(Co) deposits, Kemerovo Oblast, Gornaya Shoriya Region Russia (Konovalenko et al. 2012). Very recently, the occurrence of hibonite and grossite samples from an exotic mineralization from Sierra de Comechingones, San Luis, Argentina has been reported; in addition to dellagiustaite (a new mineral of the spinel supergroup, ideally $Al_2V^{2+}O_4$), hibonite and grossite are main phases (Cámara et al. 2019). Comparable rocks have been reported to occur at Mt. Carmel (northern Israel), where similar super-reduced mineral assemblages are found to have crystallized from high-*T* melts trapped in xenoliths within picritic-tholeiitic lavas ejected from Cretaceous volcanoes (Griffin et al. 2019). In both localities, hibonite is purple and occurs as centimetric euhedral phenocrystals, while grossite occurs as interstitial light violet crystals up to a few millimeters. Furthermore, crystals of both minerals frequently have tubular inclusions of a V-rich phase isostructural with a non-stoichiometric vanadium oxide (approximately V_2O) indicating very low oxygen fugacity (Griffin et al. 2020). These rocks have formed in presence of high CH_4 and H_2 fugacity as evidenced by the presence of the first ever reported metal hydride, VH_2, in nature (Bindi et al. 2019). The geology of the Argentinian locality is by contrast mostly

unknown as Sierra de Comechingones is a 100 km long formation composed of Neoproterozoic metamorphic rocks, mainly high grade migmatites, as well as Paleozoic granitoids (Cámara et al. 2019, and refs. therein), but the metamorphic grade so far recorded in bedrock exposures is too low for the formation of the peculiar mineral assemblage described above.

In addition to its geological significance, the mineral assemblage from Sierra de Comechingones offers a unique case-study on the coloration of its constituent minerals. Indeed, high concentrations of vanadium cause very unusual coloration in both hibonite and grossite, and they might be of interest in their synthetic analog forms as a tangible extension of the colorant palettes used in the ceramic pigment industry. By instance, nickel bearing hibonite has been proposed as a potential route to the development of inexpensive, enduring and cobalt-free blue ceramic pigments (Ardit et al. 2016; Li et al. 2016).

In the hibonite structure (space group $P6_3/mmc$) vanadium ions, in various valence states (divalent, trivalent, and tetravalent), may be distributed over five different polyhedra. Hibonite, with structural formula $^{[XII]}A(^{[VI]}M1^{[V]}M2^{[IV]}M3_2^{[VI]}M4_2^{[VI]}M5_6)O_{19}$, has a structural topology that can be described as a repetition of two alternating, approximately close-packed polyhedral layers parallel to (001) (Graetsch and Gebert 1995; Bermanec et al. 1996; Nagashima et al. 2010; Giannini et al. 2014; Doyle et al. 2014; Ardit et al. 2016). The cubic close-packed layer constitutes blocks that have the spinel ($S = [M_6O_8]^{2+}$) structure. These blocks are alternated by hexagonal close-packed layers (block $R = [AM_6O_{11}]^{2-}$) in a $S'RSR'S'$ sequence, where R' and S' are blocks rotated by 180° about the c-axis relative to R and S, respectively (Bermanec et al. 1996; Giannini et al. 2014; Ardit et al. 2016). Calcium cations occur in 12-fold coordination (site A), whereas the Al^{3+} ions are located at different coordination sites, including three distinct octahedra [$M1$ (point symmetry D_{3d}), $M4$ (C_{3v}), and $M5$ (C_s)], the $M3$ tetrahedron (C_{3v}), as well as an unusual trigonal bipyramid [$M2$ (D_{3h})] five-fold coordinated by oxygen ions (Bermanec et al. 1996; Hofmeister et al. 2004; Ardit et al. 2016). The polyhedral arrangement in the hibonite structure is depicted

in Figure 1, with the tetrahedral (*M*3) and octahedral (*M*1 and *M*5) polyhedra at the *S*-block, whereas the Ca site, the trigonal bipyramidal (*M*2), and the octahedral (*M*4) polyhedra at the *R*-block.

Hibonite can accommodate a wide range of ions with different valences and coordinations. The preferential polyhedral occupancies of dopants from literature are shown in Figure 1. With exception of *M*1 (very regular and small) and *M*5 (a bit distorted) octahedral sites, preferentially occupied by Al^{3+}, the cation preferential accommodation in the hibonite structure can be schematized as follows: M^{2+} ions (e.g., Mg^{2+}, Fe^{2+}, Zn^{2+}, Mn^{2+}, and Ni^{2+}) at the *M*3 tetrahedral site, M^{3+} ions (e.g., Ti^{3+}, Fe^{3+}, and V^{3+}) at the *M*2 trigonal bipyramidal site, M^{5+} ions (e.g., Sb^{5+}) at the *M*4 octahedral site, and M^{4+} ions (e.g., Ti^{4+} and Mn^{4+}) at both the *M*2 and *M*4 sites. It should be noted that presence of Ni^{2+} (up to 0.2 apfu) has been observed also at the *M*4 octahedral site (Ardit et al. 2016). The preference of divalent cations for the *M*3 site is quite peculiar, but it is possible because a M^{2+} for Al^{3+} substitution is electrostatically more favorable than the incorporation of highly charged cations, as demonstrated by consideration of Pauling bond-strength (Holtstam et al. 1995), Bond Valence calculations (Nagashima et al. 2010), and calculations of the Madelung factors for various hypothetical schemes of cation distribution (Graetsch and Gebert 1995).

Unlike hibonite, the possible locations of vanadium ions in grossite are limited to two crystallographically independent tetrahedral sites. A polyhedral representation of the grossite structure (space group *C*2/*c*) is provided in Figure 2.

In the grossite structure (structural formula $^{[VII]}A(^{[IV]}T1^{[IV]}T2)_4O_7$), Ca is sevenfold coordinated at the *A* site (C_2 site symmetry, pseudo-C_{2v}), while Al is distributed over two tetrahedral sites (*T*1 and *T*2, both C_1 site symmetry), with *T*2 being slightly more distorted than *T*1 (Goodwin and Lindop 1970). Grossite has a crystal structure related to those of feldspar minerals but, unlike feldspars, it contains no tetrahedral silicon atoms to provide a charge balancing mechanism. For this reason, one of the four O atoms in grossite is triclustered with three tetrahedrally coordinated Al cations (Fig. 2*b*), and the remaining O

atoms form Al–O–Al bridges with one or two Ca^{2+} neighbors for charge compensation (Ponomarev et al. 1971; Stebbins et al. 2001).

The present investigation is aimed at determination of the mechanisms responsible for the unusual coloration in both hibonite and grossite found in the mineral assemblage from Sierra de Comechingones by means of a combined approach which entails EMPA analysis, single crystal X-ray diffraction and optical absorption spectroscopy.

EXPERIMENTAL METHODS

Specimen description

Single-crystal specimens were extracted from a crushed rock chip. Hibonite is present as deep red plate hexagonal crystals, which are yellowish pink in thin sections, showing frequent tubular inclusions of native vanadium rimmed by dellagiustaite (Griffin et al. 2020). Figure 3 shows the detail of a transverse section of a hibonite crystal. A grain that is free of inclusions and has homogenous coloration was checked under a microscope and chosen for successive experiments.

Grossite constitutes the rock matrix and is purplish pink, strongly pleochroic, and it shows frequent inclusions of dellagiustaite and an Al-rich perovskite (Fig. 4) (Cámara et al. 2019). A suitable large crystal that is free of inclusions was chosen under a microscope for later analyses.

Chemical analyses

EMPA. Chemical compositions of the hibonite and grossite specimens were determined using a JEOL 8200 Super Probe electron microprobe analyzer (EMPA) operating in X-ray wavelength-dispersive mode (WDS-EMPA). Operating conditions included an accelerating voltage of 15 kV, beam current of 5 nA, beam diameter of 1 μm, peak counting-time 30 s, and 10 s of counting time for

background at both sides of the peak.. Corrections of the raw data were made with the Φ(ρZ) procedures (Pouchou and Pichoir 1985). Spectral lines, analyzing crystals, and standards used were: F *Kα* (LDE1, hornblende 123), S *Kα* (PET, galena), V *Kα* (LIF, metallic vanadium), Sr *Kα* (PET, celestine), Na *Kα* (TAP, omphacite 154), Ti *Kα* (LIF, ilmenite 149), Mn *Kα* (LIF *Kα*, rhodonite), Cl *Kα* (PET, scapolite), Mg *Kα* (TAP, olivine 153), La *Lα* (LIF, synthetic $LaPO_4$), Fe *Kα* (LIF, fayalite 143), K *Kα* (PET, K-feldspar), Al *Kα* (TAP, grossular), Ce *Lα* (LIF, synthetic $CePO_4$), Ca *Kα* (TAP, grossular), Si *Kα* (TAP, grossular), Cr *Kα* (LIF, metallic Cr), and Ba *Lα* (LIF, sanbornite). Overlap corrections of V on Ti, and Cr on V were applied. Detection limits (in ppm) were F 599, S 259, V 299, Sr 350, Na 240, Ti 291, Mn 331, Cl 119, Mg 146, La 598, Fe 292, K 103, Al 180, Ce 588, Ca 147, Si 143, Cr 325, and Ba 321. The analytical results for hibonite and grossite (mean results of eight spot analyses) are given in Table 1.

(LA)-ICP-MS. Trace element compositions were determined by laser ablation (LA)-ICP-MS at the IGG-CNR-UOS of Pavia (Italy). The instrument couples a 266 nm Nd:YAG laser microprobe (Brilliant, Quantel) with a quadrupole ICP-MS system (DRCe from PerkimElmer). The NIST-SRM612 and ^{43}Ca were used as external and internal standards, respectively. Accuracy and precision, achieved using a USGS reference sample BCR 2, are better than 10% and 5%, respectively. Data reduction was carried out using the Glitter software package (Griffin et al., 2008) and and the obtained results are listed in Table 2.

Single-crystal X-ray diffraction

Single-crystal XRD data for hibonite were collected at room temperature on a four-circle κ-geometry Rigaku XtaLAB Synergy diffractometer, operating at 50 kV and 1 mA, with a monochromatized Mo*Kα* radiation and equipped with a Hybrid Pixel Array detector at 62 mm from the sample position. Data for grossite were collected at room temperature on a four-circle κ-geometry Rigaku SuperNova diffractometer at the Dipartimento Terra e Ambiente (Università di Pavia, Italy), operating at 50 kV and

1 mA, with a monochromatized Mo$K\alpha$ radiation and equipped with a Pilatus 200K detector at 68 mm from the sample position. A combination of ω / ϕ scans were used to maximize redundancy and data coverage. Images were acquired in shutterless mode with a step scan of 0.5° and an exposure time of 0.5 s per frame for hibonite and with a step scan of 0.5° and exposure times of 0.28 and 1.14 s at low and high θ, respectively, per frame for grossite. Crystal structures were refined using SHELX-2018 (Sheldrick 2015), starting from the atomic coordinates of Nagashima et al. (2010) for hibonite, and Goodwin and Lindop (1970) for grossite; neutral scattering curves were employed. Fourier difference maps did not reveal any maximum over 0.59 e^- $Å^{-3}$ for hibonite, and 0.91 e^- $Å^{-3}$ for grossite. Experimental details, atom coordinates and equivalent isotropic atom displacement parameters, anisotropic displacement parameters, and bonding and geometrical parameters are reported in supplemental Tables S1,S2,S3,S4 for hibonite and supplemental Tables S5,S6,S7,S8 for grossite. Crystallographic information files, including structure factor lists, have been deposited as electronic supplemental material.

Optical absorption spectroscopy

Polarized, room-temperature optical-absorption spectra (OAS) in the range 333–1000 nm (30,000–10,000 cm^{-1}) were recorded at a spectral resolution of 1 nm on doubly polished single-crystal sections (thicknesses in the range 57 to 68 µm) using an AVASPEC-ULS2048 × 16 spectrometer attached via a 400 µm UV optical fiber cable to a Zeiss Axiotron UV-microscope. A 75 W Xenon arc lamp was used as a light source, and Zeiss Ultrafluar 10× lenses served as an objective and condenser. The diameter of the circular aperture was 200 µm. A UV-quality Glan–Thompson prism with a working range from 250 to 2700 nm (40,000 to 3704 cm^{-1}) was used as a polarizer. The wavelength scale of the spectrometer was calibrated against Ho_2O_3-doped and Pr_2O_3/Nd_2O_3-doped standards (Hellma glass filters 666F1 and 666F7).

In the spectral range 1000-5000 nm (10,000-2000 cm^{-1}) a Bruker Vertex 70 FTIR spectrometer equipped with a halogen-lamp source and a CaF_2 beam-splitter, coupled to a Hyperion 2000 microscope with a ZnSe wire-grid polarizer and an InSb detector, was used for spectrum collections.

The collected OAS have been deposited as electronic supplemental material.Band positions and intensities were obtained by fitting the spectra using the Fityk software (Wojdyr 2010) with Gaussian peak shape functions; the energy (position) precisions of absorption bands are estimated to be at least 30 cm^{-1}.

RESULTS AND DISCUSSION

Crystal structure

The sample of hibonite studied by single crystal X-ray diffraction shows a composition in close agreement with its chemical analysis, $(Ca_{1.01}Na_{0.01})_{\Sigma 1.02}(Al_{11.31}V_{0.55}Ti_{0.03}Mg_{0.11}Si_{0.01})_{\Sigma 13.01}O_{19.}$ In particular, the structure refinement shows that V is mainly ordered over $^{[V]}M2$ and $^{[VI]}M4_2$ sites with compositions $^{M2}(Al_{0.95}V_{0.05})$ and $^{M4}(Al_{1.79}V_{0.21})$, respectively, and to a lesser extent at the $^{[VI]}M5_6$ site with composition $^{M5}(Al_{5.94}V_{0.06})$; Mg is ordered at the $^{[IV]}M3_2$ site with composition $^{M3}(Al_{1.88}Mg_{0.12})$. The small amount of Ti probably occupies the *M*4 site. The incorporation of Ti^{4+} in hibonite is frequent in meteorites where it is counter balanced by Mg. In the studied sample, both Ti^{4+} and Mg are very low and their charges are counterbalanced within error (0.11 and 0.03 apfu for Mg^{2+} and Ti^{4+}, respectively). It is therefore expected that V is mainly in trivalent oxidation state, thus replacing homovalently Al^{3+} at *M*2 and *M*4 sites, and in a lesser amount (ca. 1%) at *M*5 site. This site occupancy would lead to the following formula: $Ca_{1.00}(Al_{11.56}V_{0.29}Mg_{0.12}Ti_{0.03})_{\Sigma 13}O_{19.}$ The *M*2 site is very particular as it can be considered a half occupied trigonal bipyramid with two possible configurations (Figs. 5*a* and 5*b*), or in a four-fold coordination as a disordered tetrahedron half occupied in the cell (Fig. 5*c*). This has been discussed by

Nagashima et al. (2010), who explored the possibility of dynamic disorder by low-temperature single-crystal X-ray diffraction using a gem crystal from Myanmar. Since no temperature-dependence of the mean-square displacement values for the *M*2 site parallel to *c* (U_{33}) was observed, a static disorder mechanism, which is related to local configurations at the *M*2 site and associated cation substitution (Ti^{4+} in their sample), has been adopted. The U_{33} determined here is half the value of Nagashima et al. (2010), but the amount of substitution in their sample is more than three times that in our sample, namely $^{M2}(Al_{0.83}Ti^{4+}_{0.17})$ vs. $^{M2}(Al_{0.95}V_{0.05})$ for Nagashima et al.'s and our hibonite samples, respectively. It seems improbable that V^{3+} enters into a site with fourfold coordination because this cation usually avoids this type of coordination, e.g., see coulsonitic spinels or the recently found dellagiustaite where V^{3+} and V^{2+} occupy octahedral sites (Cámara et al. 2019), and therefore this possibility needs to be further explored by optical spectroscopy.

Structural refinement of grossite yielded different tetrahedral site sizes: ⟨*T*1–O⟩ = 1.758 Å (with V_{poly} = 2.76 $Å^3$ and polyhedral distortion, TAV = 30.4°[2]), and ⟨*T*2–O⟩ = 1.769 Å (with V_{poly} = 2.78 $Å^3$ and polyhedral distortion, TAV = 54.7°[2]). The small amount of V cations found by EMPA (0.03 apfu) are probably hosted at the *T*2 site. However, as mentioned above, V^{3+} usually avoids tetrahedral coordination. Due to longer bond distances and a higher degree of polyhedral distortion V^{3+} is likely to be located at the *T*2 site. Incidentally, the *T*2 sites form double chains along *c* lattice and perpendicular to *b* lattice (and thus *β*), whereas *T*1 sites form single chains parallel to the previous. The configuration of these chains makes that a "short" distance (2.671 Å) is present across the base of the *T*2 sites with an out-of-coordination O1 anion, along aprox [401] (Fig. 6). This configuration could turn out convenient locally for a V^{3+} defect at *T*2 sites, that would have a 4+1 configuration.

In addition, the color and the strong pleochroism observed in the grossite samples from Argentina must be related to a particular stress situation that can be best investigated by optical absorption spectroscopy.

Optical absorption spectroscopy

The room-temperature optical absorption spectra of the V-bearing hibonite sample are shown in Figure 7, in which E||E denotes spectra recorded with plane-polarized light vibrating along the crystallographic *c*-axis and E||O spectra obtained perpendicular to this direction. The recorded spectra of V-bearing hibonite are characterized by a set of broad absorption bands spanning the entire near infrared to UV spectral range (Fig. 7). The large number of absorption bands, their broadness, and their wide range of spectral energies suggest that vanadium cations occur in more than one valence states and/or in several types of coordination polyhedra with highly variable sizes and/or symmetries. In order to analyze the spectra in more detail we fitted the spectra with peaks of Gaussian shape (Fig. 8). The fitting results are summarized in Table 3 together with our tentative band assignments.

Our chemical analyses of the studied hibonite crystals show only one transition metal element, vanadium, in detectable concentrations. Consequently, only vanadium cations can contribute to the sample color through absorption caused by electronic *d-d* transitions. Based on previous investigations on V-bearing compounds (Low 1957; Pryce and Runciman 1958; McClure 1962; Weber and Riseberg 1971; Schmetzer 1982; Carlson and Rossman 1988; Burns 1993), we assign the most intense absorption bands at 24,860 and 17,980 cm^{-1} to the spin-allowed electronic *d-d* transitions $^3T_{1g}(^3F) \rightarrow ^3T_{1g}(^3P)$ and $^3T_{1g}(^3F) \rightarrow ^3T_{2g}(^3F)$ in octahedrally-coordinated V^{3+}, respectively. The calculated crystal field splitting parameter ($10Dq$ = 19,160 cm^{-1}) and interelectronic repulsion parameter (Racah B = 538 cm^{-1}) are in excellent agreement with those observed for octahedrally V^{3+} in other oxides (Pryce and Runciman 1958; McClure 1962; Schmetzer 1982; Carlson and Rossman 1988; Burns 1993). The shapes of these two strong bands are asymmetric, suggesting that V^{3+} is located in a MO_6-polyhedron characterized by site symmetry lower than O_h. For instance, the band assigned to the $^3T_{1g}(^3F) \rightarrow ^3T_{2g}(^3F)$ in octahedrally-coordinated V^{3+} (band *c*) displays a prominent shoulder at ~19,600 cm^{-1}. Comparable band asymmetries have been observed for the spin-allowed *d-d* bands in optical spectra of Cr^{3+}-bearing hibonite compounds

(Medina et al. 2017). The asymmetries of the two strong bands (*c* and *e*) display in our hibonite spectra can be explained by small to moderate energy splittings of the excited states caused by a symmetry decrease of the crystal field around the absorbing V^{3+}. Similar effects have been recorded in spectra of, e.g., V^{3+} in a crystal field of C_{3v} symmetry in corundum (Pryce and Runciman 1958; McClure 1962; Burns 1993), and Cr^{3+} in a D_{3d} crystal field in spinels (Hålenius et al. 2010). The proposed assignments of the strong bands (*c* and *e*) are in good agreement with the strong V^{3+}ordering at the six-coordinated *M*4-site with local symmetry C_{3v}, as determined by our structure refinement of hibonite. Low intensity bands caused by the spin-forbidden *d-d* transitions $^3T_{1g}(^3F) \rightarrow {}^1A_{1g}$ to $^3T_{1g}(^3F) \rightarrow {}^1E_1, {}^1T_{2g}$ in V^{3+} at the *M*4-site are predicted, on the basis of the previously reported *Dq*- and *B*-values, to occur at ~19,500 cm^{-1} and 10,500 cm^{-1}, respectively. We fail to record these bands because they are masked by much stronger spin-allowed *d-d* bands that occur at nearby energies. Similarly, we do not observe any discrete absorption bands caused by electronic *d-d* transitions in V^{3+} at the remaining *M*-sites (*M*1, *M*2, *M*3 and *M*5). We cannot exclude their presence, but as the V cation concentrations at those sites are low in our sample, the intensities of any potential bands caused by such absorbing species would be masked by the strong bands caused by transitions in V^{3+} at the *M*4-site.

Burns and Burns (1984) as well as Ihinger and Stolper (1986) concluded that Fe^{2+}, Fe^{3+} and Ti^{3+} were enriched at the 5-coordinated cation site in hibonite, and they suggested that this would also imply the enrichment of V^{3+} at that site. Inspired by their suggestion we explored whether V^{3+} at the 5-coordinated *M*2-site would potentially contribute to the spectra of our hibonite sample by testing several different band assignment models. However, they all resulted in unrealistic values for the spectroscopic *Dq*- and *B*-parameters. The least anomalous values were obtained for a model that assigned the band shoulder at 19,600 cm^{-1} as well as an inferred absorption band coinciding with the 24,860 cm^{-1} band to V^{3+} at the *M*2-site. However, the obtained *Dq*-value of 2100 cm^{-1} using this model is unrealistically high and the derived Racah *B*-parameter of 445 cm^{-1} is too low for V^{3+}.

In addition to the absorption bands discussed above, we observe strong and distinctly polarized absorption bands centered at 9930 (9630 and 10,230 cm^{-1}, along O and E, respectively), 14,410 cm^{-1} and 21,855 cm^{-1}. These bands occur at energies that are not compatible with V^{3+} in six-coordinated polyhedra. Furthermore, distinctive absorption bands attributable to V^{3+} in tetrahedral coordination occur at energies below 8000 cm^{-1} and no such bands are observed in our hibonite spectra. Consequently, we suggest that these strong bands (*a, b* and *d*), with all the characteristics of bands caused by spin-allowed electronic *d-d* transitions, are due to V^{2+} at octahedrally coordinated sites (Sturge 1963; Smith 1969; Mei et al. 2014). Applying the Tanabe-Sugano energy level diagram for V^{2+} ($3d^3$ electron configuration) in octahedral coordination (Tanabe and Sugano 1954), these absorption bands can be assigned to transitions from the ground state $^4A_{2g}(^4F)$ to the excited states $^4T_{2g}(^4F)$, $^4T_{1g}(^4F)$ and $^4T_{1g}(^4P)$. Along with the results from single-crystal XRD analysis, the strong polarization of the bands in the near infrared region suggests that V^{2+} is hosted at the *M*4 face-sharing octahedral site. The calculated crystal field splitting parameter ($10Dq$ = 9930 cm^{-1}; corresponding to the energy of the $^4A_{2g}(^4F) \rightarrow {}^4T_{2g}(^4F)$ spin-allowed transition) and interelectronic repulsion parameter (Racah B = 433 cm^{-1}; obtained from the separation of the $^4T_{1g}(^4F)$ and $^4T_{1g}(^4P)$ levels) result in a Dq/B-ratio of 2.29, which compares well with a value of 1.85 reported for octahedrally coordinated V^{2+} by Hughes et al. (2011).

The room-temperature absorption spectra of grossite from Sierra de Comechingones (Figs. 9 and 10) show several intense and strongly polarized absorption bands in the visible spectral (at ~17,400, ~22,000, and ~25,400 cm^{-1}) and near infrared (at ~9200 and ~10,700 cm^{-1}) regions. According to our chemical analyses of this sample, vanadium is the only transition metal element present in detectable concentrations. Consequently, the recorded absorption bands must be caused by electronic *d-d* transitions in vanadium cations.

Based on previous spectra of tetrahedrally coordinated V^{3+} in ~~grossite and~~ other compounds (Weber and Riseberg 1971; Mikhailov et al. 1993; Kück and Jander 1999; Kammoun 2002; Brik et al. 2006; Ma et

al. 2006), we assign the most intense bands in our grossite spectra to spin-allowed *d-d* electronic transition of tetrahedrally-coordinated V^{3+}.

From the Tanabe-Sugano energy level diagram for a $3d^2$ cation as V^{3+} in tetrahedral coordination (Tanabe and Sugano 1954), the absorption bands at 7520 and 9275cm^{-1} (av. 8400 cm^{-1}), those at 10,720, 12,170, and 14,460 cm^{-1} (av. 12,450 cm^{-1}), and those centered at 17,340, 19,330, and 21,930 cm^{-1} (av. 19,530 cm^{-1}) can be assigned to transitions from the ground state $^3A_{2g}(^3F)$ to the excited states $^3T_{2g}(^3F)$, $^3T_{1g}(^3F)$ and $^3T_{1g}(^3P)$. The band observed at 25410 cm^{-1}, is due to a transition to the $^1T_2(^1G)/^1E(^1G)$ energetic level (see Table 4).

The calculated crystal field strength ($10Dq$ = 8400 cm^{-1}, corresponding to the energy of the $^3A_{2g}(^3F) \rightarrow {}^3T_{2g}(^3F)$ spin-allowed transition) and interelectronic repulsion (Racah B = 444 cm^{-1}) parameters are in agreement with those reported for V^{3+}-doped $Y_3Al_5O_{12}$, $LiGaO_2$, and $LiAlO_2$ oxides (Mikhailov et al. 1993; Kück and Jander 1999).

Lack of information on the geometric relations between crystallographic and optical main axes makes the determination from recorded optical spectra of the V^{3+} distribution among the two available tetrahedrally coordinated sites inconclusive.

Color

The color of the present hibonite and grossite along their main optical directions (O and E; and X, Y and Z, respectively) was determined by calculating the respective xy-values in the CIE 1931 color space from the measured polarized single crystal spectra. The positions of the calculated chromaticity values are summarized in the CIE 1931 color space chromaticity diagram (Figure 11).

In terms of the Munsell color system, hibonite is yellowish pink and grossite is purplish pink. Grossite is distinctly pleochroic with Y > Z > X. It is almost colorless in the optical X-direction, but displays a

characteristic purplish pink color in the Y- and Z-directions. The pleochroic scheme of hibonite is O > E, with a yellowish pink color in the E-direction and pink color in the O-direction.

The contents of ions that can impart color to hibonite and grossite crystals (such as Cr, Co, Ni) are smaller than 5 ppm (Table 2). Hence, the unusual coloration observed in the investigated specimens is related to the presence of chromophoric vanadium cation species.

IMPLICATIONS

Vanadium is one of the most dispersed elements in the Earth's crust (Huang et al. 2015). This may be explained by its preferential partitioning into the metallic core portion of the Earth at high pressure and low fO_2 conditions during the "deep magma ocean" process (Palme and O'Neill 2003). Vanadium is a transition metal element with multiple valence states (from V^{2+} to V^{5+}) in oxides, silicate minerals, and melts (Sutton et al. 2005), and a large amount of V^0 enters the metallic core (McDonough and Sun 1995). This fact explains an increasing interest in V as an indicator of geochemical evolution. The vanadium oxidation state in planetary materials is an oxygen fugacity index, which spans over 8 orders of magnitude (in $\log fO_2$) within the solar system (Papike et al. 2005). In addition, vanadium has two stable isotopes (^{51}V and ^{50}V) with relative abundances of ~99.76% and ~0.24%, respectively (Shore et al. 2010). Theoretical and experimental studies have documented fractionation of isotopes of multi-valence elements during redox reactions (Ellis et al. 2002; Schauble et al. 2004; Wu et al. 2015; Wu et al. 2016). For vanadium isotopes, variations which span more than 2‰ for Earth materials have been observed,

whereas Earth materials are always heavier than any other meteorite ever studied (Nielsen et al. 2019, and refs. therein). Thus, V isotopic compositions of terrestrial samples might serve as a fingerprint of redox-state variations in petrogenetic processes. For instance, positive correlations of ^{51}V as a function of Si content in basalts have been ascribed to isotope fractionation between V^{3+} and V^{4+} which show different partitioning behaviours between crystal and melt (Mallmann and O'Neill 2009). Yet, V content is inversely correlated to Si content (Huang et al. 2015). On the other hand, as stated by Papike et al. (2005), the understanding of vanadium valence-state partitioning over crystallographic sites and phases is still in its infancy. It is important to determine valence states and site distributions of cations in mineral phases using advanced techniques (e.g., XANES) (Papike et al. 2005). Using optical absorption spectroscopy, we have demonstrated that vanadium can easily be hosted by the hibonite structure via substitution schemes already observed for cations with a higher valence, e.g., Ti^{4+}. In particular, it is observed that, at very reducing conditions, V^{2+} can be incorporated into the hibonite *M*4 octahedral sites. Note that the speciation of V^{2+} cannot be detected by XANES spectroscopy as no signal is observed at the V pre-edge in V^{2+}-bearing materials (Sutton et al. 2015). The observation of the presence of V^{2+} in hibonite could open an interesting subject of study for this mineral as an indicator of reducing conditions (i.e., low Eh) during the growth of particular mineralogical assemblages. It is worth to note that in samples from Sierra de Comechingones grossite crystallizes after hibonite and the V is only in V^{3+} oxidation state, whereas it assumes both divalent and trivalent valence state in hibonite (as well as in dellagiustaite; Cámara et al. 2019). In addition, reduction of V is also favored by low pH conditions (Huang et al. 2015), which may provide essential information in hydrothermal systems. It may be argued that the rarity of hibonite (and grossite) in Earth environments would limit their potential applications in Geosciences. However, calcium aluminates are indeed important phases being among the first to crystallize during the early stages of the solar nebula condensation, where they formed inclusions (CAI)

in carbonaceous chondrites. Again, the recent description of the hibonite occurrence in terrestrial rocks having different origins (Griffin et al. 2020) open further scenarios.

In addition, the incorporation of vanadium into the structures of hibonite and grossite exerts very different chromatic effects, mostly due to the different coordinations and symmetries of the electronic environment of V^{3+}. Albeit at limited concentration levels, the occupancy of V^{3+} at tetrahedrally coordinated sites in grossite leads to strong color effects, which are not expected for hibonite, in which V^{3+} is in octahedral coordination. This particular feature may be exploited in pigment manufacture, where both the hardness and ceramic behavior of calcium aluminate phases present decisive advantages.

Acknowledgments

We thank Matteo Alvaro (University of Pavia) for access to the Rigaku Supernova diffractometer, and Massimo Tiepolo (University of Milano) and Antonio Langone (IGG-CNR-UOS of Pavia) for trace element determination by laser ablation (LA)-ICP-MS. FC acknowledges financial support by the grant "Ricerca Locale 2014", Università di Milano. FC and MA acknowledge financial support by the grant from the Italian Ministry of Education (MIUR) through the project "Dipartimenti di Eccellenza 2018–2022".We thank Prof. George Rossman and an anonymous reviewer for constructive reviews.

References

Ardit, M., Borcănescu, S., Cruciani, G., Dondi, M., Lazău, I., Păcurariu, C., and Zanelli, C. (2016) Ni-Ti codoped hibonite ceramic pigments by combustion synthesis: Crystal structure and optical properties. Journal of the American Ceramic Society, 99, 1749–1760.

Beckett, J.R., Live, D., Tsay, F.-D., Grossman, L., and Stolper, E. (1988) Ti^{3+} in meteoritic and synthetic hibonite. Geochimica et Cosmochimica Acta, 52, 1479–1495.

Bermanec, V., Holtstam, D., Sturman, D., Criddle, A.J., Back, M.E., and Šćavničar S. (1996) Nežilovite, a new member of the magnetoplumbite group, and the crystal chemistry of magnetoplumbite and hibonite. Canadian Mineralogist, 34, 1287–1297.

Bindi, L., Cámara, F., Griffin, W.L., Huang, J.-X., Gain, S.E.M., and O'Reilly, S.Y. (2019) The discovery of the first natural hydride. American Mineralogist, 104, 611–614.

Brearley, A.J., and Jones, R.H. (1998) Chondritic Meteorites. In J.J. Papike, ed., Planetary Materials, 36, 3-001–3-398. Reviews in Mineralogy and Geochemistry, Mineralogical Society of America, Chantilly, Virginia.

Brik, M.G., Avram, N.M., and Avram, C.N. (2006) Crystal field energy level structure of $LiAlO_2:V^{3+}$ and $LiGaO_2:V^{3+}$. Spectrochimica Acta Part A, 63, 759–765.

Burns, R.G. (1993) Mineralogical applications of crystal field theory, 2nd ed., 576 p. Cambridge University Press, Cambridge, U.K.

Burns, R.G., and Burns, V.M. (1984) Crystal chemistry of meteoritic hibonites. Journal of Geophysical research, 89, C313–C321.

Cámara, F., Bindi, L., Pagano, A., Pagano, R., Gain, S.E.M., and Griffin, W.L. (2019) Dellagiustaite: A novel natural spinel containing V^{2+}. Minerals, 9, 4–19.

Cao, Z-M., Qin, S., Bi, Yu-R., and Wang, J.-W. (1997) The discovery and preliminary study of hibonite from Handan Xingtai area, Hebei Province. Acta Petrologica et Mineralogica, 16, 353–356.

Carlson, W.D., and Rossman, G.R. (1988) Vanadium- and chromium-bearing andalusite: Occurrence and optical-absorption spectroscopy. American Mineralogist, 73, 1366–1369.

Delbos, L. (1955) Note sur le gisement d'un minéral nouveau "la hibonite" de l'Androy Mandrareen. Rapport Annuel du Service Géologique pour 1955, 143–144. Antananarivo, Madagascar.

Doyle, P.M., Schofield, P.F., Berry, A.J., Walker, A.M., and Knight, K.S. (2014) Substitution of Ti^{3+} and Ti^{4+} in hibonite ($CaAl_{12}O_{19}$). American Mineralogist, 99, 1369–1382.

Ellis, A.S., Johnson, T.M., and Bullen, T.D. (2002) Chromium isotopes and the fate of hexavalent chromium in the environment. Science, 295, 2060–2062

Giannini, M., Boffa Ballaran, T., and Langenhorst, F. (2014) Crystal chemistry of synthetic Ti-Mg-bearing hibonites: A single-crystal X-ray study. American Mineralogist, 99, 2060–2067.

Goodwin, D.W., and Lindop, A.J. (1970) The crystal structure of $CaO \cdot 2Al_2O_3$. Acta Crystallographica, B26, 1230–1235.

Graetsch, H., and Gebert, W. (1995) Cation distribution in magnetoplumbite type $SrTi_6Co_6O_{19}$. Zeitschrift für Kristallographie, 210, 9–13.

Griffin, W.L., Powell, W., Pearson, N.J. and O'Reilly, S.Y. (2008) GLITTER: data reduction for laser ablation ICP-MS. In Sylvester, O. ed. Mineralogical Association of Canada Short Course Series. Vancouver, British Columbia, 40, 2004-207.

Griffin, W.L., Gain, S.E.M., Cámara, F., Bindi, F., Shaw, J., Alard, O., Saunders, M., Huang, J.-X., Toledo, V., and O'Reilly, S.Y. (2020) Extreme reduction: Mantle-derived oxide xenoliths from a hydrogen-rich environment. Lithos, 358-359, 105404.

Griffin, W.L., Gain, S.E.M., Huang, J.-X., Saunders, M., Shaw, J., Toledo, V., and O'Reilly, S.Y. (2019) A terrestrial magmatic hibonite-grossite-vanadium assemblage: Desilication and extreme reduction in a volcanic plumbing system, Mount Carmel, Israel. American Mineralogist, 104, 207–219.

Gross, S. (1977) The Mineralogy of the Hatrurim Formation, Israel. Geological Survey of Israel Bulletin, 70, 80 p.

Halenius, U., Andreozzi, G.B., and Skogby, H. (2010) Structural relaxation around Cr^{3+} and the red-green color change in the spinel (sensu stricto)-magnesiochromite ($MgAl_2O_4$-$MgCr_2O_4$) and gahnite-zincochromite ($ZnAl_2O_4$-$ZnCr_2O_4$) solid-solution series. American Mineralogist, 95, 456–462.

Hazen, R.M., Papineau, D., Bleeker, W., Downs, R.T., Ferry, J.M., McCoy, T.J., Sverjensky, D.A., and Yang, H. (2008) Mineral evolution. American Mineralogist, 93, 1693–1720.

Hofmeister, A.M., Wopenka, B., and Locock, A.J. (2004) Spectroscopy and structure of hibonite, grossite, and $CaAl_2O_4$: Implications for astronomical environments. Geochimica et Cosmochimica Acta, 68, 4485–4503.

Holtstam, D. (1996) Iron in hibonite: a spectroscopic study. Physics and Chemistry of Minerals, 23, 452–460.

Holtstam, D., Norrestam, R., and Sjödin, A. (1995) Plumboferrite: New mineralogical data and atomic arrangement. American Mineralogist, 80, 1065–1072.

Huang, J.-H., Huang, F., Evans, L., and Glasauer, S. (2015) Vanadium: Global (bio)geochemistry. Chemical Geology, 417, 68–89.

Hughes, M.A., Curry, R.J., and Hewak, D.W. (2011) Determination of the oxidation state and coordination of a vanadium doped chalcogenide glass. Optical Materials, 33, 315–322.

Ihinger, P.D., and Stolper, E. (1986) The color of meteoritic hibonite: an indicator of oxygen fugacity. Earth and Planetary Science Letters, 78, 67–79.

Kammoun, S. (2002) Crystal-field analysis of the V^{3+} excitation spectrum in $LiGaO_2$ and $LiAlO_2$ oxide crystals. Physica Status Solidi B, 232, 306–313.

Konovalenko, S.I., Ananyev, S.A., and Garmayeva, S.S. (2012) Rare and new minerals of the Tashelgin-Maiza zone of Mountain Shoria, their features and nature. Engineering & Technologies, 5, 301–310.

Kück, S., and Jander, P. (1999) Spectroscopic properties of the tetrahedrally coordinated V^{3+} ion in oxide crystals. Optical Materials, 13, 299–310.

Laville, F., Perrin, M., Lejus, A.M., Gasperin, M., Moncorge, R., and Vivien, D. (1986) Synthesis, crystal growth, structural determination, and optical absorption spectroscopy of the magnetoplumbite type compound $LaNiAl_{11}O_{19}$. Journal of Solid State Chemistry, 65, 301–308.

Li, J., Medina, E.A., Stalick, J.K., Sleight, A.W., and Subramanian, M.A. (2016) Colored oxides with hibonite structure: A potential route to non-cobalt blue pigments. Progress in Solid State Chemistry, 44, 107–122.

Low, W. (1957) A note regarding the spectrum of V^{3+} complexes in octahedral fields. Zeitschrift fur Physikalische Chemie, 13, 107–110.

Ma, C., Kampf, A.R., Connolly, H.C., Beckett, J.R., Rossman, G.R., Sweeney Smith, S.A., and Schrader D.L. (2011) Krotite, $CaAl_2O_4$, a new refractory mineral from the NWA 1934 meteorite. American Mineralogist, 96, 709–715.

Ma, J., Du, M., and Miao, F. (2006) Spectroscopic investigation of YAG crystal doped with tetrahedrally coordinated V^{3+} ions. Physica Status Solidi B, 243, 1785–1790.

Maaskant, P., Coolen, J.J.M.M.M., and Burke, E.A.J. (1980) Hibonite and coexisting zoisite and clinozoisite in a calc-silicate granulite from southern Tanzania. Mineralogical Magazine, 43, 995–1003.

Mallmann, G., and O'Neill, H.S.C. (2009) The crystal/melt partitioning of V during mantle melting as a function of oxygen fugacity compared with some other elements (Al, P, Ca, Sc, Ti, Cr, Fe, Ga, Y, Zr and Nb). Journal of Petrology, 50, 1765–1794.

McClure, D.S. (1962) Optical spectra of transition-metal ions in corundum. The Journal of Chemical Physics, 36, 2757–2779.

McDonough, W.F., and Sun, S.-S. (1995) The composition of the earth. Chemical Geology, 120, 223–253.

Medina, E.A., Li, J., and Subramanian, M.A. (2017) Colored oxides with hibonite structure II: Structural and optical properties of $CaAl_{12}O_{19}$-type pigments with chromophores based on Fe, Mn, Cr and Cu. Progress in Solid State Chemistry, 45, 9–29.

Mei, Y., Zheng, W.-C., and Zhang, L. (2014) Unified calculations of the optical band positions and spin-Hamiltonian parameters for V^{2+} ions in $CdCl_2$ crystal. Molecular Physics, 112, 982–986.

Mikhailov, V.P., Kuleshov, N.V., Zhavoronkov, N.I., Prokohsin, P.V., Yumashev, K.V., and Sandulenko, V.A. (1993) Optical absorption and nonlinear transmission of tetrahedral V^{3+} (d^2) in yttrium aluminum garnet. Optical Materials, 2, 267–272.

Momma, K., and Izumi, F. (2011) VESTA 3 for three-dimensional visualization of crystal, volumetric and morphology data. Journal of Applied Crystallography, 44, 1272–1276.

Nagashima, M., Armbruster, T., and Hainschwang, T. (2010) A temperature-dependent structure study of gem-quality hibonite from Myanmar. Mineralogical Magazine, 74, 871–885.

Nielsen, S.G., Auro, M., Righter, K., Davis, D., Prytulak, J., Wu, F., and Owens, J.D. (2019) Nucleosynthetic vanadium isotope heterogeneity of the early solar system recorded in chondritic meteorites. Earth and Planetary Science Letters, 505, 131–140.

Palme, H., and O'Neill, H.S.C. (2003) Cosmochemical estimates of mantle composition. Treatise on Geochemistry, 2, 1–38.

Papike, J.J., Karner, J.M., and Shearer, C.K. (2005) Comparative planetary mineralogy: valence state partitioning of Cr, Fe, Ti, and V among crystallographic sites in olivine, pyroxene, and spinel from planetary basalts. American Mineralogist, 90, 277–290.

Ponomarev, V.I., Kheiker, D.M., and Belov, N.V. (1971) Crystal structure of calcium dialuminate, CA2. Soviet Physics-Crystallography, 15, 995–998.

Pouchou, J.L., and Pichoir, F. (1985) 'PAP' Φ(ρZ) procedure for improved quantitative microanalysis. In J.T. Armstrong, Ed., Microbeam Analysis, p. 104–106. San Francisco Press, San Francisco, California.

Pryce, M.H., and Runciman, W.A. (1958) The absorption spectrum of vanadium corundum. Discussions of the Faraday Society, 26, 34–42.

Schauble, E., Rossman, G.R., and Taylor H.P. Jr. (2004) Theoretical estimates of equilibrium chromium-isotope fractionations. Chemical Geology, 205, 99–114.

Schmetzer, K. (1982) Absorption spectroscopy and colour of V^{3+}-bearing natural oxides and silicates -A contribution to the crystal chemistry of vanadium. Neues Jahrbuchl für Mineralogie - Abhandlungen, 144, 73–106.

Shore, A., Fritsch, A., Heim, M., Schuh, A., and Thoennessen, M. (2010) Discovery of the vanadium isotopes. Atomic Data and Nuclear Data Tables, 96, 351–357.

Sheldrick, G.M. (2015) Crystal structure refinement with SHELXL. Acta Crystallographica, C71, 3–8.

Smith, W.E. (1969) Single-crystal absorption spectra of crystal field bands of bivalent vanadium ions in vanadium dichloride and related environments at low temperatures. Journal of the Chemical Society A, 2677–2682.

Stebbins, J.F., Oglesby, J.V., and Kroeker, S. (2001) Oxygen triclusters in crystalline $CaAl_4O_7$ (grossite) and in calcium aluminosilicate glasses: ^{17}O NMR. American Mineralogist, 86, 1307–1311.

Sturge, M.D. (1963) Optical spectrum of divalent vanadium in octahedral coordination. Physical Review, 130, 639–646.

Sutton, S.R., Karner, J., Papike, J., Delaney, J.S., Shearer, C., Newville, M., Eng, P., Rivers, M., and Dyar, M.D. (2005) Vanadium K edge XANES of synthetic and natural basaltic glasses and application to microscale oxygen barometry. Geochimica and Cosmochimica Acta, 69, 2333–2348.

Tanabe, Y., and Sugano, S. (1954) On the absorption spectra of complex ions. I and II. Journal of the Physical Society of Japan, 9, 753–779.

Taylor, H. (1997) Cement Chemistry, 2nd ed., 480 p. Thomas Telford Ltd., London, U.K.

Ulianov, A., Kalt, A., and Pettke, T. (2005) Hibonite, $Ca(Al,Cr,Ti,Si,Mg,Fe^{2+})_{12}O_{19}$, in granulite xenoliths from the Chyulu Hills volcanic field, Kenya. European Journal of Mineralogy, 17, 343–356.

Utsunomiya, A., Tanaka, K., Morikawa, H., and Marumo, F. (1988) Structure refinement of $CaO_6 \cdot Al_2O_3$. Journal of Solid State Chemistry, 75, 197–200.

Weber, M.J., and Riseberg, L.A. (1971) Optical spectra of vanadium in yttrium aluminum garnet. Journal of Chemical Physics, 55, 2032–2038.

Weber, D., and Bischoff, A. (1994) Grossite ($CaAl_4O_7$) - a rare phase in terrestrial rocks and meteorites. European Journal of Mineralogy, 6, 591–594.

Wild, M., and Milisenda, C.C. (2013) Hibonit aus Myanmar (Burma). Zeitschrift der Deutschen Gemmologischen Gesellschaft, 62, 25–30 (in German).

Wojdyr, M. (2010) Fityk: a general-purpose peak fitting program. Journal of Applied Crystallography, 43, 1126–1128.

Wu, F., Qin, T., Li, X.F., Liu, Y., Huang, J.H., Wu, Z.Q., and Huang, F. (2015) First-principles investigation of vanadium isotope fractionation in solution and during adsorption. Earth and Planetary Science Letters, 426, 216–224.

Wu, F., Qi, Y.H., Yu, H.M., Tian, S.Y., Hou, Z.H., and Huang, F. (2016) Vanadium isotope measurement by MC-ICP-MS. Chemical Geology, 421, 17–25.

FIGURE CAPTIONS

Figure 1. Polyhedral representation of the two structural layers: the hexagonal close-packed *R*-block (i.e., Ca, trigonal bipyramidal *M*2, and octahedral face-sharing *M*4 sites) and the cubic close-packed *S*-block (i.e., layers of *M*5 octahedra interspaced by the *M*3 tetrahedra and *M*1 octahedra), of the hibonite structure in a perspective view along [110] (modified after Ardit et al. 2016). Ca (white sphere) is twelve-fold coordinated by O3 ×6 and O5 ×6. On the right side, a representation of each polyhedron with its respective ligands and the occupancy of dopants from literature (Burns and Burns 1984; Ihinger and Stolpe, 1986; Laville et al. 1986; Beckett et al. 1988; Utsunomiya et al. 1988; Graetsch and Gebert 1995; Holtstam et al. 1995; Holtstam 1996; Bermanec et al. 1996; Hofmeister et al. 2004; Nagashima et al. 2010; Giannini et al. 2014; Doyle et al. 2014; Ardit et al. 2016). Figure was drawn with Vesta 3.4.6 (Momma and Izumi 2011).

Figure 2. Polyhedral representation of the grossite structure in a perspective view along [101] (*a*). Tricluster structure based on three Al tetrahedra that share one oxygen atom per molecular unit (*b*). Figures were drawn with Vesta 3.4.6 (Momma and Izumi 2011).

Figure 3. Detail of hibonite crystals (hib) in a thin section showing the tubular native vanadium (V^0) inclusions rimmed by dellagiustaite in several growing sequences, and an inclusion-depleted rim. In the upper and lower left fields of the picture light violet grossite (gro) show inclusions of idiomorphic dellagiustaite crystals (dgt), as well as blebs of native vanadium rimmed by dellagiustaite.

Figure 4. Detail of the matrix of the rock showing pleochroic grossite (gro) associated with dellagiustaite (dgt) and perovskite (pv) in a thin section.

Figure 5. Detail of the *M*2 site in hibonite showing the long-range average configuration (*a*), possible local environments of five-fold coordination with a long bond (*b*) and four-fold coordination (*c*). The distance between the two *M*2 sites is 0.381(4) Å.

Figure 6. Double chains of *T*2 tetrahedra and adjacent single chains of *T*1 tetrahedra in grossite. A short *T*2–O1 distance along [401] is shown. Figure was drawn with Vesta 3.4.6 (Momma and Izumi 2011).

Figure 7. Room-temperature polarized absorption spectra of a hibonite single-crystal from Sierra de Comechingones (doubly polished sections of 63 μm thick).

Figure 8. Peak deconvolution of hibonite single-crystal optical spectra along E (*a*) and O (*b*).

Figure 9. Room-temperature polarized absorption spectra of a grossite single-crystal from Sierra de Comechingones (doubly polished sections of 57 μm thick along X and Y, and 68 μm thick along Z).

Figure 10. Peak deconvolution of grossite single-crystal optical spectra along X (*a*), Y (*b*), and Z (*c*).

Figure 11. Chromaticity values in the CIE 1931 color space chromaticity diagram for hibonite and grossite along their main optical directions (O and E; and X, Y and Z, respectively).

TABLES

Table 1. Chemical analytical data for grossite (Grs) and hibonite (Hib) single-crystals in oxide weight percent (wt.%) and recalculated on the basis of 7 and 19 oxygen atoms, respectively.

	Grs	Hib		Grs	Hib
			No. O atoms	7	19
SiO_2	0.06	0.09	Si	0.00	0.01
TiO_2	b.d.l.	0.35	Ti	0.00	0.03
Al_2O_3	77.35	85.24	Al	3.96	11.31
V_2O_3	0.74	6.12	V	0.03	0.55
MgO	0.03	0.63	Mg	0.00	0.11
CaO	21.84	8.41	Ca	1.02	1.01
Na_2O	0.07	0.04	Na	0.01	0.01
Total	100.09	100.88	Cations sum	5.02	13.03

b.d.l. = beyond detection limit

Table 2. LA-ICP-MS data for grossite (Grs) and hibonite (Hib) single-crystals in ppm (mean results of three spot analyses and their standard deviation, s.d.). Values beyond the detection limit (b.d.l.) have been excluded from the calculation of the average values.

Element	mass	Grs	s.d.	Hib	s.d.	Element	Mass	Grs	s.d.	Hib	s.d.
Li	7	0.55	0.20	b.d.l.		Ba	138	3.77	0.24	5.37	0.23
Be	9	2.08	1.23	1.54	0.91	La	139	0.26	0.05	4.31	0.20
B	11	13.34	6.40	11.82	3.83	Ce	140	0.39	0.06	7.42	0.30
Mg	25	397.62	18.60	1472.24	48.84	Pr	141	0.05	0.02	0.83	0.05
Si	29	2100.44	242.99	3413.70	227.25	Nd	146	b.d.l.		2.94	0.21
Ca	43	150087.22	5083.75	60034.88	1739.41	Sm	149	1.12	0.34	0.51	0.15
Ca	44	143424.40	4954.57	57868.33	1655.11	Eu	151	b.d.l.		b.d.l.	
Sc	45	b.d.l.		1.30	0.20	Gd	157	0.34	0.09	0.45	0.10
Ti	49	127.80	8.21	502.99	18.74	Tb	159	0.07	0.02	0.06	0.02
V	51	4343.78	152.14	13200.89	382.53	Dy	163	0.29	0.10	0.53	0.08
Cr	53	b.d.l.		6.80	1.42	Ho	165	0.05	0.02	0.09	0.02
Co	59	0.24	0.06	0.33	0.06	Er	167	0.24	0.10	0.28	0.08
Ni	60	b.d.l.		0.82	0.19	Tm	169	0.06	0.02	0.04	0.01
Zn	66	2.37	1.26	3.70	0.91	Yb	173	0.32	0.19	b.d.l.	
Rb	85	0.14	0.04	0.19	0.04	Lu	175	0.06	0.02	0.03	0.01
Sr	88	45.42	2.88	63.99	2.90	Hf	177	b.d.l.		0.67	0.11
Y	89	1.42	0.13	1.25	0.08	Ta	181	b.d.l.		0.09	0.02
Zr	90	0.32	0.10	11.24	0.48	Pb	208	1.23	0.15	0.24	0.05
Nb	93	b.d.l.		0.05	0.02	Th	232	0.03	0.01	0.98	0.07
Cs	133	b.d.l.		b.d.l.		U	238	0.09	0.04	0.83	0.06

Table 3. Spectroscopic properties of V ions in the hibonite sample obtained by curve-fitting of room-temperature spectra.

	Site	Local symmetry	Transition	Label	Energy* cm^{-1}	Average cm^{-1}	FWHM* cm^{-1}	Polarization, relative intensities
V^{3+}	*M*4	C_{3v}	$^3T_{1g}(^3F) \rightarrow {}^3T_{2g}(^3F)$	*c*	17,980		2410	E > O
			$^3T_{1g}(^3F) \rightarrow {}^3T_{1g}(^3P)$	*e*	24,860		3540	E > O
Crystal field strength, 10*Dq*					19,160			
Racah *B*					538			
V^{2+}	*M*4	C_{3v}	$^4A_{2g}(^4F) \rightarrow {}^4T_{2g}(^4F)$	*a*	9630 10,230	9930	1880 1940	O E
			$^4A_{2g}(^4F) \rightarrow {}^4T_{1g}(^4F)$	*b*	14,410		2540	O
			$^4A_{2g}(^4F) \rightarrow {}^4T_{1g}(^4P)$	*d*	21,860		2720	E = O
Crystal field strength, 10*Dq*					9930			
Racah *B*					433			

*The reported energies and FWHMs are numerical averages over the two optical directions.

Table 4. Spectroscopic properties of tetrahedrally coordinated V^{3+} ions in the grossite sample obtained by curve-fitting of room-temperature spectra.

	Site	Local symmetry	Transition	Label	Energy* cm^{-1}	Average cm^{-1}	FWHM* cm^{-1}	Polarization, relative intensities
V^{3+}	*T*2	C_1	$^3A_{2g}(^3F) \rightarrow {}^3T_{2g}(^3F)$	*a*	7520 9275	8400	1910 2000	X > Z Y > X > Z
			$^3A_{2g}(^3F) \rightarrow {}^3T_{1g}(^3F)$	*b*	10,720 12,170 14,460	12,450	1520 1950 3030	X > Y > Z Z > Y X > Y
			$^3A_{2g}(^3F) \rightarrow {}^3T_{1g}(^3P)$	*c*	17,340 19,330 21,930	19,530	2360 2590 3320	Y > Z ≈ X Z ≈ X ≈ Y X ≈ Y > Z
			$^3A_{2g}(^3F) \rightarrow {}^1T_{2g}(^1G)/{}^1E(^1G)$	*d*	25,410		2880	Y > X
Crystal field strength, 10*Dq*					8400			
Racah *B*					444			

*The reported energies and FWHMs are numerical averages over the three optical directions.

Fig. 1

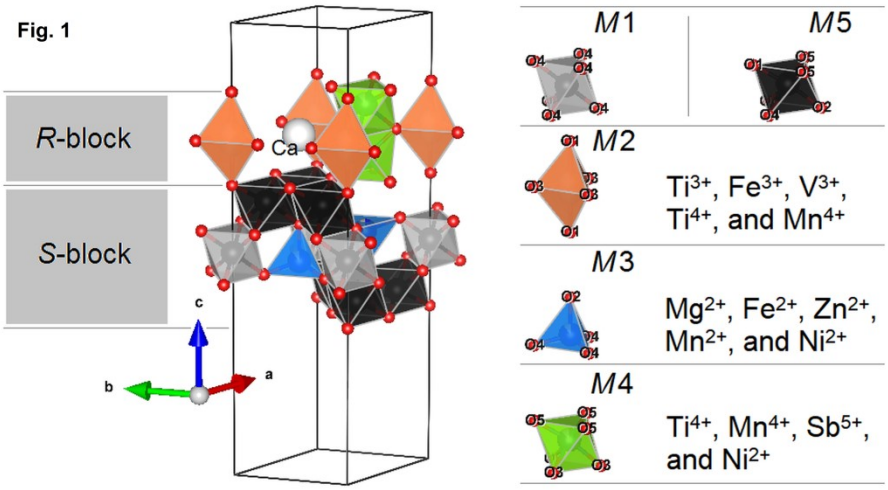

Fig. 2a

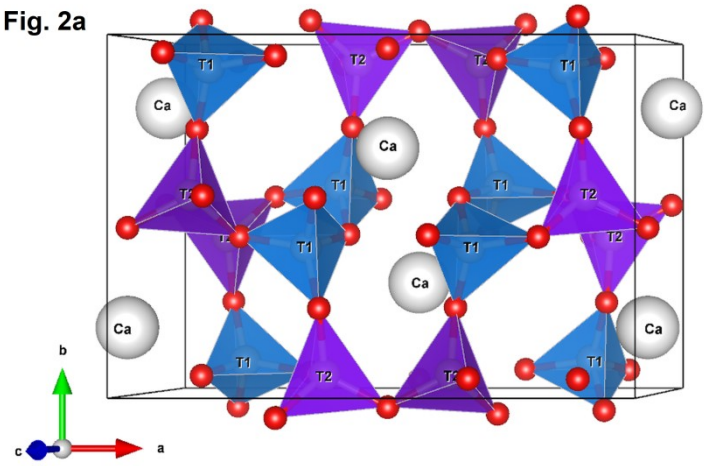

Fig. 2b

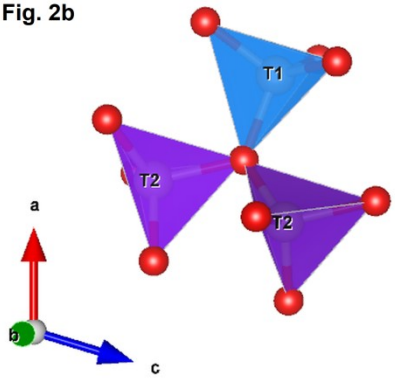

Fig. 3

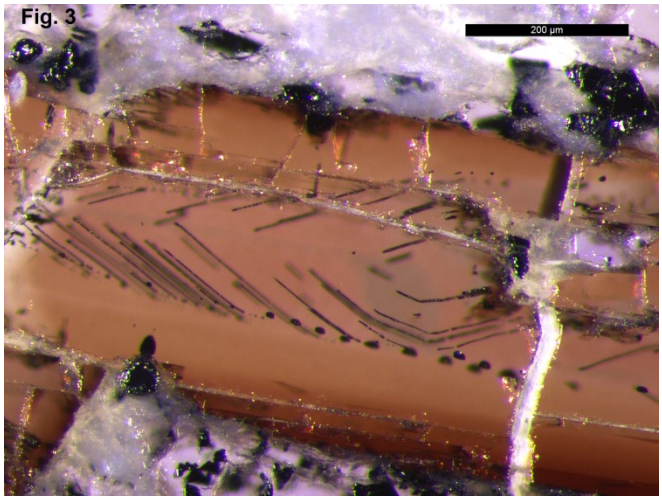

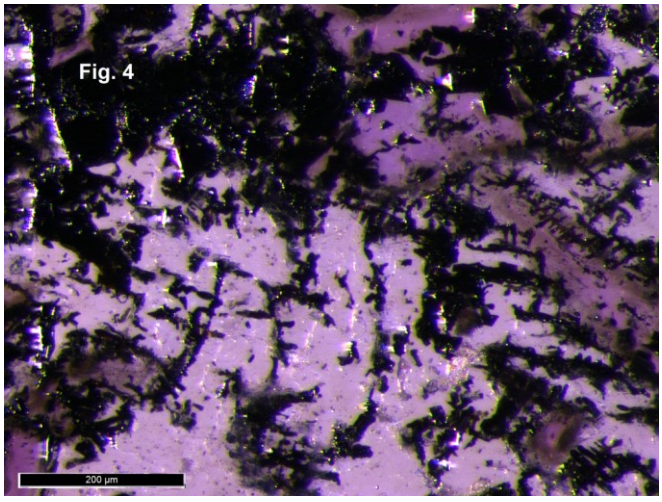

Fig. 5a

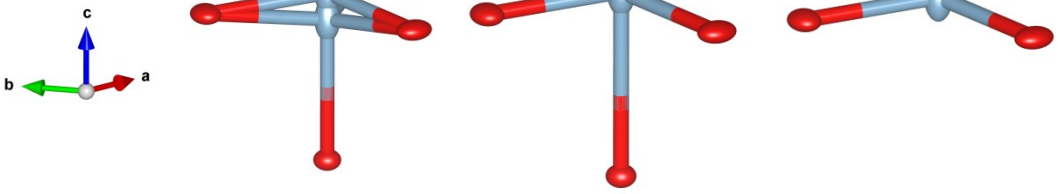

Fig. 5b

Fig. 5c

Fig. 6

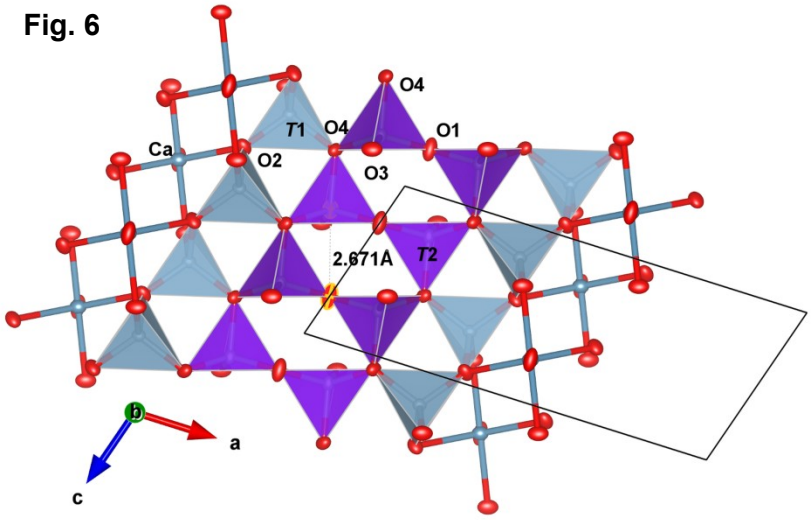

Fig.7

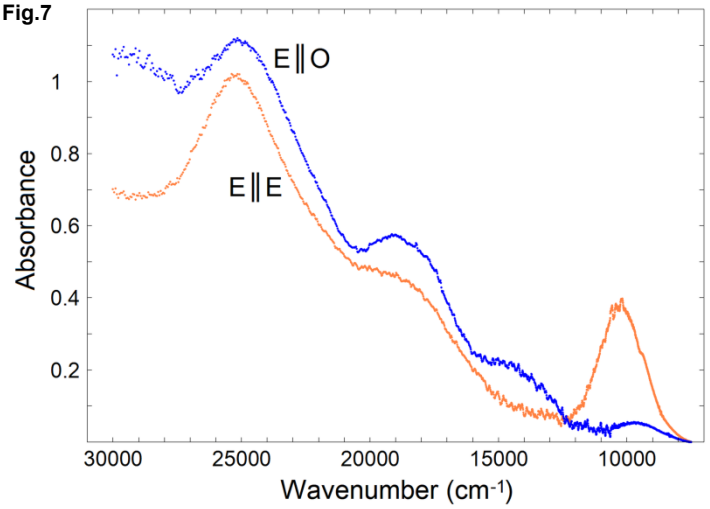

Fig.8a

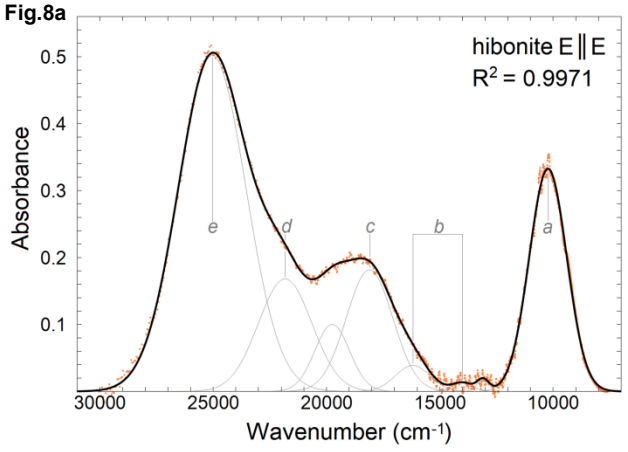

Fig.8b

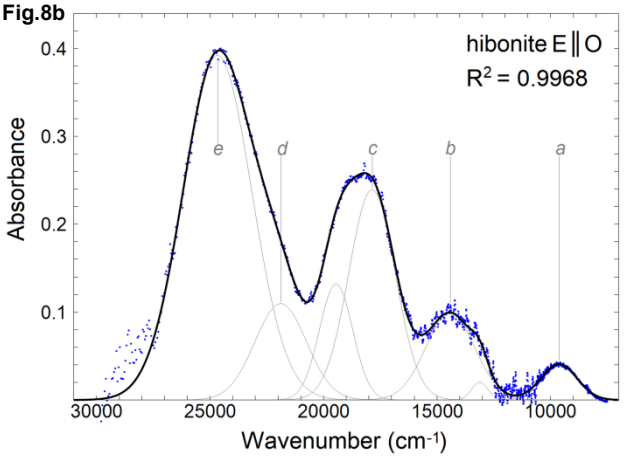

Fig.9

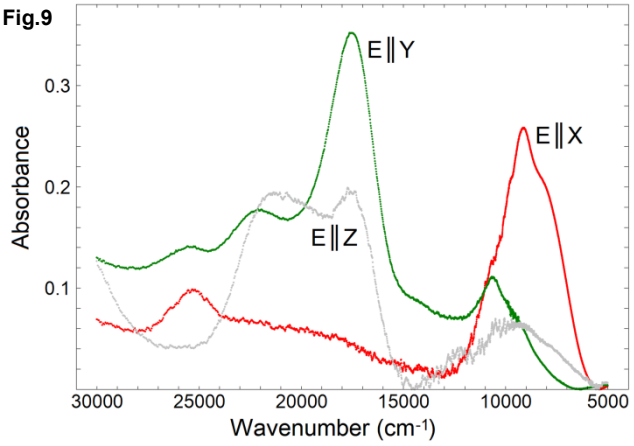

Fig.10a

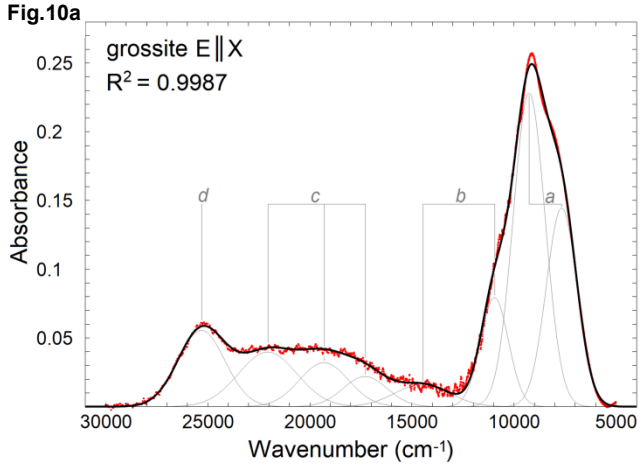

Fig.10b

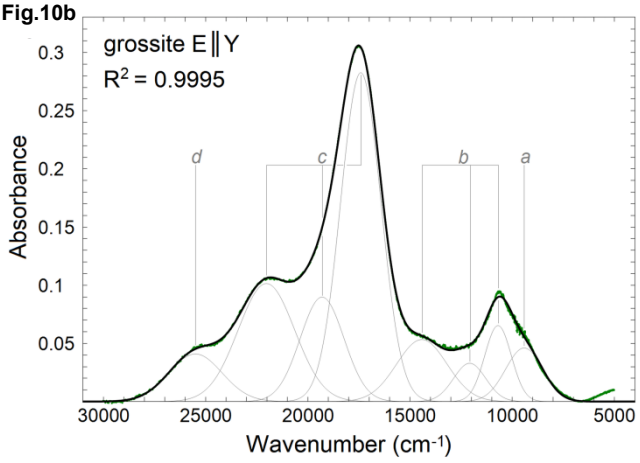

Fig.10c

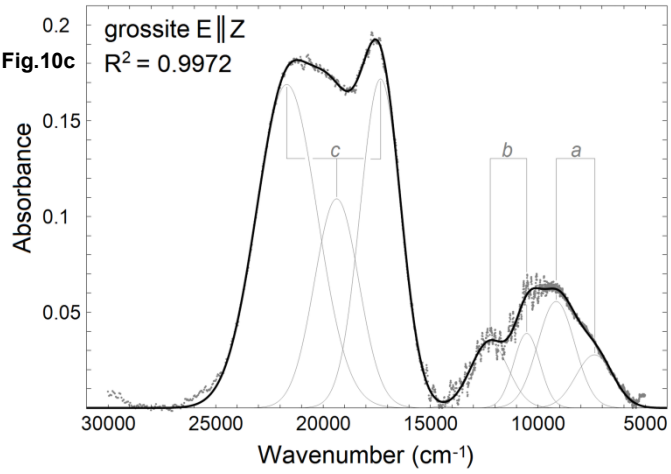

Fig.11